Title

Intercalation of Mg into a Few-Layer Phyllomanganate in Nonaqueous Electrolytes at Room Temperature

Journal

Chemistry of Materials, 32(14)

ISSN

0897-4756

Authors

Kwon, Bob Jin
Kim, Chunjoong
Jokisaari, Jacob R
et al.

Publication Date

2020-07-28

DOI

10.1021/acs.chemmater.0c01305

Intercalation of Mg into a Few-Layer Phyllomanganate in Non-aqueous Electrolytes at Room Temperature

Bob Jin Kwon[†,‡,§], Chunjoong Kim[‖], Jacob R. Jokisaari[§,⊥], Hyun Deog Yoo[#], Sang-Don Han[‡,§], Soojeong Kim[‡,§], Ka-Cheong Lau[‡,§], Yi-Sheng Liu[¶], Jinghua Guo[¶], Baris Key[‡,§], Robert F. Klie[§,⊥], and Jordi Cabana[†,§*]

[†]Department of Chemistry, University of Illinois at Chicago, Chicago, IL 60607, United States

[‡]Chemical Sciences and Engineering Division Argonne National Laboratory Argonne, IL 60439, United States

[§]Joint Center for Energy Storage Research, Argonne National Laboratory, Lemont, IL 60439, United States

[‖]School of Materials Science and Engineering, Chungnam National University, Daejeon, 305-764, Republic of Korea

[⊥]Department of Physics, University of Illinois at Chicago, Chicago, IL 60607, United States

[#]Department of Chemistry and Chemical Institute for Functional Materials, Pusan National University, Busan 46241, Republic of Korea

[¶]Advanced Light Source, Lawrence Berkeley National Laboratory, Berkeley, CA 94720, United states

KEYWORDS

Mg intercalation, Vernadite, Phyllomanganate, nanocrystalline, defects, lattice water

ABSTRACT

The use of oxide cathodes in Mg batteries would unlock a potential energy storage system that delivers high energy density. However, poor kinetics of Mg diffusion in known solid oxide lattices strongly limits reversible intercalation, which motivates the sustained exploration of new candidates. Herein, nanocrystals of a few-layered phyllomanganate, reminiscent of the mineral vernadite, were shown to have considerable electrochemical activity toward Mg intercalation at room temperature, where it delivered ~190 mAh/g at ~1.9 V (*vs* Mg/Mg^{2+}) in batteries paired with a Mg metal anode. Multimodal characterization confirmed the notable degree of reversible intercalation by probing the structural, compositional and redox changes undertaken by the oxide. Distinct levels of Mg activity were also observed while varying the content of small amounts of lattice water and the temperature of the reaction. The results reaffirm the prospects for operational Mg batteries using oxide cathodes in moderate conditions, overcoming current limits of performance of this prospective technology.

INTRODUCTION

Rechargeable, non-aqueous Mg batteries have been considered as an alternative to Li-ion technology with potential to deliver high energy density at low cost.[1-3] However, their promise strongly relies on the discovery of cathode materials with high and reversible storage capacity at high redox potential, to fulfill the requirements of energy density against the benchmark of the dominating Li-ion devices.[4, 5] Reversible intercalation of Mg^{2+} has been attempted in diverse host compounds such as metal chalcogenides, polyanionic olivines, and organic compounds.[6-12] Among these candidates, frameworks composed of soft anions, especially Mo_6X_8 (X=S, Se) and TiS_2, are capable of repeated electrochemical cycling when paired with a Mg anode at moderate temperatures.[8, 13] Whereas these phases are suitable for reversible intercalation of Mg^{2+}, their low operating potentials and specific capacities severely limit their practical application. Theoretically, both metrics could be raised using oxide frameworks instead, while preserving structural flexibility that enables and sustains percolating pathways for Mg^{2+} migration at all states of charge.[6, 14, 15] However, despite extensive efforts over two decades, there is a glaring absence of oxide hosts with a sufficiently notable degree of reversible activity, particularly when paired with a Mg metal anode in non-aqueous electrolytes. Sluggish migration is assigned as the main cause of such poor electrochemical properties, due to pathways that show relatively high barriers to cation hopping owing to the existence of strong electrostatic interactions in the presence of localized charges.[16, 17] The situation is consequently even worse at moderate temperatures, with overpotentials so large as to open up alternate pathways for electrochemical

conversion instead, where the oxide is reduced by losing O^{2-} rather than by intercalating Mg^{2+},[18, 19] but these alternative pathways are inherently plagued by irreversibility and energy inefficiency. As a result, the development of a competitive Mg battery is at much earlier stage compared to Li-based technologies, underpinned by the need of foundational, rather than developmental, advances. Chief among them is the question of whether intercalation of the divalent ion into a transition metal oxide is fundamentally possible at high potential, compared to softer chalcogenides, and moderate temperature, in non-aqueous electrolytes.

Layered oxides constitute one possible family of hosts favorable for intercalation of ions since their two-dimensional geometry can be tuned to a variety of interlayer spacings, offering a diversity of sites that could potentially accommodate multivalent cations. Among them, manganese oxides combine simple synthetic methods with large flexibility both in structure and accessible oxidation states of Mn, constituting a good platform to gather fundamental knowledge on the intercalation chemistry of multivalent ions.[20, 21] Birnessite-type A_xMnO_2 consists of a collection of sheets of edge-sharing MnO_6 octahedra units with ~7 Å of interlayer spaces, where water and cations (A) occupy the interlayer to compensate charge balances.[22] The presence of water molecules in the host framework is a common means to enhance the kinetics of intercalation of Mg^{2+}, by shielding the effective charges of ions in the lattice from each other.[23-25] However, whereas birnessite has been reported to intercalate Mg^{2+} in aqueous electrolytes, it was also found to undergo a conversion mechanism in non-aqueous Mg^{2+} electrolytes, involving a rearrangement of the transition metal sub-lattice to form frameworks reminiscent of a spinel structure,[19] even when controlled amounts of water were added to the solutions.[25] On one hand, the large atomic rearrangement involved in the conversion reaction compromises reversibility.

On the other hand, the intentional use of water in the electrolyte is precluded in a full-cell configuration for high energy density because of its incompatibility with a Mg metal anode[26] and its a low anodic stability. The origin of the difference in behavior depending on the nature of the electrolyte has not been fully ascertained. In any case, these results highlight the need to explore strategies such that the kinetics of Mg^{2+} intercalation in non-aqueous electrolytes can be enhanced to bypass a pathway of conversion of the active oxide. Structural modification through introduction of defects is predicted to significantly affect the kinetics of Mg^{2+} intercalation in oxides,[15, 27] pointing at a worthwhile path of exploration. Encouragingly, introduction of defects was recently found to enhance the electrochemical deintercalation of Mg^{2+} from $MgCr_2O_4$.[28]

Atomic defects can be introduced into the extended birnessite framework by controlling the method of growth, either in the form of vacancies or interstitial cations.[29] Beyond these point defects, as a sub-variety of birnessite, vernadite is composed of a framework showing large levels of extended crystallographic (turbostratic) disorder in the layer-stacking direction with a domain size of coherent scattering often ~10 Å.[30] Absence of coherence in the layer-stacking direction can also be achieved by exfoliating the phyllomanganate, so that few layers are present in each nanocrystal.[31] The absence of registry between layers would alter the topology and, thus, the energetic landscape between possible migration sites with Mg^{2+} in a favorable manner. While beneficial outcomes of this effect have been postulated from a broad theoretical perspective,[15] it has not been fully explored yet. Furthermore, the resulting nanocrystals would also offer shorter lengths of bulk diffusion and increase the contact area with the electrolyte, both of which could trivially enhance the kinetics of the reaction.[28, 32]

Here we introduce a nanocrystalline phyllomanganate containing only a few layers, a mixed valence of Mn and extensive interlayer defects, to facilitate Mg^{2+} migration in the lattice.[33-35] Characterization of key states when such host oxide was cycled in non-aqueous electrolytes reveals structural, compositional and electronic changes of the bulk that are consistent with reversible intercalation of the Mg^{2+} ions rather than conversion and/or amorphization.[18, 19, 21] The observations of the mechanisms are contrasted with previous studies on other phyllomanganates with different degrees of defects, water content and valence state of Mn, suggesting that they have a critical role in the activity. Aside from its inherent ability to intercalate the divalent ion, the oxide could also be paired with a Mg metal anode in non-aqueous electrolytes to build a full cell exhibiting an operating potential of ~1.8 V (*vs* Mg/Mg^{2+}) and a discharge capacity of ~190 mAh/g at room temperature. These observations constitute a fundamental step forward in the ability of oxides to reversibly intercalate Mg^{2+} ions. They enrich our understanding of Mg^{2+} intercalation electrochemistry and reach an important milestone in the long quest toward a high-energy battery based on these multivalent cations by achieving activity in an oxide at room temperature.

RESULTS

A nanocrystalline phyllomanganate, referred to here MnO_x, was synthesized via an aqueous sol-gel route involving a reduction of sodium permanganate, followed by treatment in acid to induce interlayer defects.[36] The diffraction patterns of pristine MnO_x (Figure 1a) indicated a highly disordered, poorly crystalline structure with broad reflections at *d*-spacing of ~2.42 Å,

with a long tail at higher angles, and ~1.42 Å, corresponding to (11, 20) and (31, 02) families of planes (e.g., "11" refers to (11*l*) reflections), using conventions in the literature.[34] The quotient in *d*-spacing (~1.70) was close to √3 and only a very small bump at ~19° (~4.67 Å), corresponding to (*00l*) reflections, was present, with no other discernible shoulders at low angles (Figure S1), denoting an overall hexagonal symmetry.[29, 37] Lastly, there was a broad hump between 50° and 55°, corresponding to *d* between 1.82 and 1.67 Å. Overall, the XRD pattern was reminiscent of the mineral vernadite, a form of layered phyllomanganate with very short coherent lengths along the *c*-axis.[22] The very low intensity of (*00l*) basal reflections is indicative of coherence only at the level of 5 or less single layers.[35, 38] The shoulders observed on both principal diffraction bands, together with the broad hump at 50-55°, are consistent with a defective structure composed of octahedral Mn vacancies in the layers, with the corresponding Mn cations displaced to the interlayer spacing above or below these vacancies.[29]

The amount of water in the pristine state was estimated by thermal analysis (Figure S2a). The mass loss was assumed to be due to the removal of H_2O which existed in the lattice and/or on the surface of a compound with formula $MnO_2 \cdot nH_2O$, leading to n~0.6, a value comparable to the literature.[39] It is possible that the loss also has a contribution from lattice protons instead of H_2O, which could not be evaluated directly. Above ~550 ℃, the compound transformed to α-MnO_2 (Figure S1b). A sample with low H_2O content, DH-MnO_x, was prepared by calcination at 400 ℃ for 3 hours to evaluate the effect of lattice water/protons; around half of the initial water/ proton content was removed, as shown in Figure S2a. Consistent with the removal of water at the interlayer, the most intense peaks in the XRD pattern of DH-MnO_x were comparable to the initial material, but showed a slight shift to higher angles, implying reduced *d*-spacings. Nonetheless, a

set of broad peaks with very low intensity was observed at spacings consistent with α-MnO_2 (Figure S3), which possibly indicates the sample was collected at the early onset of the transformation. Transmission electron microscopy showed highly exfoliated layers of MnO_x in the form of rolled nanosheets, consisting of 5~6 layers of the oxide with a length of 20~30 nm. (Figure 1b, d). The short length along the *c*-axis due to the presence of few layers would induce very short coherent scattering along that dimension, which, coupled with the existence of stacking defects between these layers, would be consistent with the absence of (*00l*) reflections in the patterns. Even after calcination at 400 ℃, the morphologies were retained, but highly porous structures with multiple nano-domains were introduced (Figure 1c, e).

The electrochemical properties were first measured in a half-cell consisting of a carbon cloth reference and MnO_x working electrode with an ionic liquid electrolyte, $Mg(TFSI)_2$-PY14TFSI, while varying the temperature of the cells to probe reaction kinetics (Figure 2). The cathodic reaction at room temperature proceeded from ~0.35 V and a discharging capacity of ~165 mAh/g was achieved at -1.4 V (Figure 2a), which could be calibrated to a potential of ~0.8 V *vs* Mg/Mg^{2+} following methods in the literature.[11] The profile was overall sloping, centered at -0.25 V *vs* carbon (~2.0 V *vs* Mg/Mg^{2+}, Figure 2c). The capacity upon the first discharge dropped to ~70 mAh/g at C/10 (Figure S4). Upon subsequent charging, a specific capacity of ~125 mAh/g was reached up to 1.3 V *vs* carbon (~3.5 V *vs* Mg/Mg^{2+}), the reaction being centered at ~1.0 V (Figure 2c). In the next cycle, the redox reactions were slightly washed out and shifted to higher potentials. The cycling curve of MnO_x at room temperature showed a gradual decrease in capacity, to ~45 mAh/g after 30 cycles (Figure 2e). The capacities in both cathodic and anodic reactions were significantly increased to 250 mAh/g and 210 mAh/g, respectively, at 50 ℃,

along with further smearing of the electrochemical profiles (Figure 2b, d). However, no clear difference in cycling retention was observed up to 30 cycles (Figure 2f). Despite the drop in capacity, the findings are encouraging in that they indicate that the reaction is not only possible, but sufficiently reversible that further incremental improvements through electrode engineering could be possible.

A full-cell was fabricated using a Mg metal anode with 0.25 M $Mg(CB_{11}H_{12})_2$ dissolved in triglyme, which has been shown to have sufficient stability up to the anodic cutoff potential.[40, 41] The cells were cycled at a rate of C/50 over the potential range of 0.5~4.4 V *vs* Mg/Mg^{2+} (Figure 3a). The resulting discharge- and charge-voltage profiles at room temperature are shown in Figure 3a. The cathodic reaction occurred mainly at ~1.9 V (*vs* Mg/Mg^{2+}), at a relatively constant potential. The subsequent anodic reaction proceeded mostly above 4.0 V, which is higher than in the half-cell experiment, possibly denoting high overpotentials due to passivating layers on the Mg metal.[42, 43] Nonetheless, the average working-potential in both types of cells was similar at 2.0~2.4 V (*vs* Mg/Mg^{2+}). The measured capacities were slightly higher than in the half-cells, at ~190 mAh/g and ~133 mAh/g for discharging and charging, respectively. The discharge capacity corresponds to approximately 0.33 moles of Mg^{2+} equivalents reacting per mole of host based on a theoretical formula MnO_2. Nonetheless, it is worth noting that XRD and spectroscopic evidence (see below) suggests that the actual x in MnO_x is below 2 due to the presence of numerous interlayer defects and vacancies, introducing large uncertainty into the calculation of capacity from coulometry. Similar activity at room temperature was achieved in a Mg full-cell with an alternative electrolyte, $Mg(TFSI)_2$ in diglyme (Figure S5), emphasizing the versatility of the oxide. The kinetics of the reaction were investigated by operating the full-cells

at 50 ℃ and 110 ℃ (Figure 3b, c). The cathodic potentials were raised with ~0.3 V between 25 ℃ and 50 ℃, along with an increase of capacity, implying improved kinetics (Figure S6). Further enhancement was not observed when operating the cell at 110 ℃, perhaps due to the onset of competing reactions. On subsequent charging, the anodic potentials were significantly lowered when raising the cell temperatures, suggesting an enhancement of kinetics upon demagnesiation (Figure 3b, c).

To evaluate the effect of the water content within the structure, the electrochemical properties of DH-MnO_x were also measured in both a half- and full-cell at varying temperatures. The discharge/charge profiles of DH-MnO_x in a half-cell at C/50 at room temperature showed that the cathodic reaction proceeded from ~0.3 V *vs* carbon and a discharge capacity of ~140 mAh/g was achieved at -1.5 V. Compared to the reactivity of MnO_x performed in the same condition (Figure 1a), a decrease of capacities of ~25 mAh/g was observed along with a relatively steep decline of cathodic curve (Figure 4a). Upon subsequent charging, a specific capacity of ~95 mAh/g was reached up to 1.2 V *vs* carbon, through a profile that showed stabilization of the anodic potential at ~0.75 V. Though both charging and discharging capacities were slightly lowered than MnO_x, significant electrochemical activity was still observed. Full cells were subsequently tested at C/50 rate over the potential range of 0.5~3.8 V (*vs* Mg/Mg^{2+}) at room temperature (Figure 4b). A discharge capacity of ~150 mAh/g was achieved at 0.5 V (*vs* Mg/Mg^{2+}), with a similar shape of the curve compared with the half-cell result. The discharge capacity corresponds to roughly 0.27 moles of Mg^{2+} per mole of a host, assuming a theoretical formula MnO_2. On subsequent charging, the slope of the electrochemical profile gradually decreased after ~3.0 V and a charge capacity of ~66 mAh/g was collected at 3.8 V (*vs* Mg/Mg^{2+}).

The lower anodic capacities in the samples after dehydration appeared to be correlated with the greater hysteresis between discharge and charge potentials. Consequently, a full-cell experiment was performed at the elevated temperature at 50 ℃ to enhance migration kinetics of Mg^{2+} (Figure 4c). An increased capacity of ~190 mAh/g compared to room temperature was observed when it was discharged to 1.0 V (vs Mg/Mg^{2+}). The anodic reaction was limited to 3.3 V vs Mg/Mg^{2+} to avoid enhanced decomposition of the electrolyte at high temperature. Despite this change, a notable increase in capacity was observed, to ~150 mAh/g, with the onset of the reaction taking place at a lower potential, mainly above ~2.5 V. The increases in both charging and discharging capacities observed at the raised temperature were thus accompanied by a reduced polarization. Given the enhanced electrochemical response at 50 ℃, characterization of electrochemical states of DH-MnO_x was conducted at this temperature.

The contents of Mg in the MnO_x electrodes harvested from half-and full-cells were estimated by TEM-EDX (Figures 5a and S7, 8). The average atomic ratio of Mg/Mn in multiple areas of discharged MnO_x particles harvested from a half-cell was 0.46 (Figure S7), higher than the value of 0.30 estimated by capacities of discharge (Figure 2a). In the full cell, the Mg/Mn ratio was 0.38 (Figure S8), compared to 0.34 estimated from the corresponding discharge capacity (Figure 3a). The elemental distribution and concentration of Mg-inserted MnO_x prepared in the full-cell experiment were evidenced by EDX mapping through the nanocrystalline particles (Figure 5a). Manganese and magnesium were detected throughout the rolled nanoparticles and the original morphology was maintained. In contrast, the Mg/Mn ratio (0.25) in magnesiated DH-MnO_x at 50 ℃ indicated a lowered value compared to MnO_x, but consistent with the estimate (0.27) from the discharged capacity (Figure 5b and S8b).

Synchrotron X-ray diffraction was measured from the same harvested electrodes. The diffraction peaks of the active materials in the electrode composites were assigned by comparing pure powder MnO_x with a composite only formed of carbon and binder, the other components in an electrode (Figure S9). The *a*- and *b*-axis planes were monitored to examine lattice alteration as a response to Mg intercalation. The high quality of the data confirmed the fine structure of the (11, 20) bands in the pristine state, as well as the existence of a very subtle hump at a *d*-spacing of 1.53 Å, which could reflect a slight distortion of the structure from a hexagonal symmetry (Figure 6 and S10).[29] The electrodes discharged to -1.4 V (*vs* carbon) in a half-cell showed a shift of (11, 20) and (31, 02) reflections to lower angles compared to the pristine pattern (Figure 6a and S10), leading to an increase of *d*-spacings to 2.47 Å and 1.43 Å, thereby increasing their ratio to 1.72 (Table 1), with no sign of new diffraction peaks. The change is consistent with a lattice expansion reminiscent of a topotactic process. This change is accompanied by the growth of the broad feature centered at a *d*-spacing of 1.53 Å, with the peak at 2.47 Å showing a selective increase in intensity at higher *d* spacing (lower diffraction angles). These changes occur when the hexagonal symmetry is lowered to orthogonal (C-centered space group),[29] as in triclinic birnessite,[44] consistent with the increase in the ratio of spacing of the two main peaks. The notable increase in intensity of the split (30*l*) reflections at 1.53 Å after reduction could reflect changes in the electron density of the corresponding planes due to the insertion of Mg^{2+}. Similar XRD changes were reported during reduction of a turbostratic hexagonal phyllomanganate, related to the one studied here, by treatment in solutions of Mn^{2+}.[33] In turn, the presence of a divalent cation like Ca^{2+} in the interlayer was found to promote reduction and introduction of the orthogonal distortion with a high intensity of the (30*l*) reflections.[33, 45]

Upon subsequent charging to 1.3 V (*vs* carbon), the reflections corresponding to (11, 20) bands reverted almost to the original *d* spacings (Figure 6a and Table 1) along with a slight increase of intensities and a return to the hexagonal symmetry of the original state. These observations indicate notable reversibility of the reaction (Figure 2a). Similar trends in structure were found in a full-cell experiment at room temperature, albeit with slightly greater shift of the peaks in both (11, 20) and (31, 02) reflection planes and, thus, significant lattice expansion after Mg^{2+} insertion (Figure 6b and Table 1), consistent with the higher capacities measured (Figure 3a). This change induced slightly greater spacing ratio of 1.73 than in the half-cell. In turn, the reversibility of the structural changes was also slightly lower in the full cell.

Compared to MnO_x, DH-MnO_x showed slightly less expansion in *d*-spacing (i.e., a smaller shift of diffraction peaks) and less increase of intensity of the split (30) band upon discharge in a full-cell, even though it was cycled at higher temperature (50 ℃ *vs* 25 ℃, Figure 6c and Table 1). After re-oxidation, the structure also reverted toward the initial state to a lesser extent than MnO_x, in terms of both peak positions and reduction of the orthogonal distortion toward hexagonal.

Mn K-edge X-ray absorption spectroscopy (XAS) was employed to understand the evolution of electronic environment in the ensemble of the electrode as a response to the electrochemical reaction. The absorption edge involves a bound state electronic transition from an occupied 1s level to empty valence 4p bands. The energy position of near-edge features is particularly sensitive to changes in shielding of nuclear charges provided by valence electrons, which tracks the formal oxidation state of the metal. Figure 7a and c presented normalized X-ray Absorption Near Edge Structure (XANES) region for pristine, discharged and charged MnO_x

electrodes prepared in a half- and full-cells at room temperature (Figure 2a and 3a), compared to two Mn standards, Mn_2O_3 (Mn^{3+}) and MnO_2 (Mn^{4+}). Following the comparison, the threshold E_0 of the Mn K-edge in the pristine electrode was slightly higher than +3. The cathodic reaction in a half-cell induced a significant shift of ~1 eV in the position of the absorption edge toward lower energy, indicating a reduction of the average oxidation states of Mn (Figure 7a, b and Table S1). The degree of reduction was slightly greater in a full- than half-cell (Table S1), as denoted by the comparison of shifts to lower energy, consistent with the changes in diffraction *d*-spacings (Figure 6 and Table 1). The formation of a predominance of Mn^{3+} leads to the cooperative Jahn-Teller distortion of the octahedral environments that induces a distortion of the phyllomanganate to an orthogonal cell,[46] as discussed in the XRD results. Upon applying an anodic current, the absorption edges shifted back to the initial position in both types of cells, denoting a reversible redox change for Mn in the bulk of the oxide electrodes. When the reactions were carried out in a full-cell, the extent of reversibility was somewhat less than the half-cell electrode, showing similar trends in the diffraction analysis and electrochemical responses.

Mn $L_{II, III}$-edge X-ray absorption spectroscopy was collected in TEY mode, which is sensitive to ~5 nm depth, providing information on the chemical state of Mn at the surface of the electrodes (Figure 8). Since the host oxide consisted of a few layers with roughly 20~30 nm length, the changes represent reactivity throughout a large volume of the nanoparticles, but they are specific only to those located at the top of the electrode, which was ~40 μm thick. The L_{II} and L_{III} edges are due to electronic transitions to the 3d bands from the $2p_{1/2}$ and $2p_{3/2}$ levels, respectively.[47] The change of the multiplet structure is attributed to the variation in symmetry of the ground state, whereas the chemical shift reflects changes in the formal redox states of Mn.

The pristine MnO_x spectrum presented intense absorption features at ~ 638.6, 639.9 and 640.6 eV, which can be associated with the existence of Mn^{2+} and Mn^{3+}. Comparison with Mn_3O_4 (Figures 8a and S11) revealed a higher intensity around 640 eV in MnO_x, indicative of a higher Mn^{3+} content, and at 641.6 eV, where intensity from Mn^{4+} is expected. Therefore, the average oxidation state slightly greater than +3 deduced from K-edge measurements results from a mixture of three different individual states. The Mn^{2+} are likely located in sites above or below octahedral cation vacancies in the manganate layer.[29] Upon reduction of MnO_x in a half-cell, the center of gravity of the spectrum significantly shifted to lower absorption energies, revealing reduced Mn valence.[48] The branching ratio, I (L_{III})/I ($L_{III} + L_{II}$), increased significantly from 0.613 to 0.689. The large branching ratio indicates the electronic environment evolved toward a high spin state of Mn ions.[49] The discharged state was close to the spectrum of MnO (Figure S11), indicating the significant formation of Mn^{2+} (high-spin d^5) on the surface of the electrode (Figure 8a). Similar changes of Mn oxidation were observed in a full-cell experiment at room temperature while a different ratio of mixed Mn states was presented in the discharged state (Figures 8b and S12a). After subsequent anodic reaction in both half- and full-cells, the spectral features and branching ratio measured by Mn $L_{II, III}$-edge XAS were comparable to the pristine state, consistent with re-oxidation (Figures 8a and b).

Although the ensemble average of the electrode surface reduced further than the bulk, individual particles showed a homogeneous change of Mn valence upon magnesiation, as revealed by the spatially resolved Mn $L_{II, III}$-edge spectra measured with electron energy loss spectra (EELS), across both pristine and magnesiated MnO_x nanocrystals (Figure S13). There was a shift of ~0.5 eV to lower energy in the Mn L_{III} peak of the magnesiated particles compared

to pristine (Figure S14), revealing a reduction of Mn.[50] However, no distinct shifts were found along individual reduced sheets, suggesting that they uniformly reacted.[50] The particles also remained uniformly crystalline, based on images from annular dark field STEM (Figure S16).. These observations further supported a mechanism of Mg^{2+} intercalation into the structure without the formation of over-reduced phases due to conversion, and subsequent amorphization of the particle surface, an alternate reaction which was observed in a different, tunnel-type manganese oxide, α-MnO_2.[18 18]

Pristine DH-MnO_x showed intense absorption features at ~638.6, ~639.3, ~639.9 and 641.6 eV, which can be associated with the mixed valences of Mn^{2+}, Mn^{3+}, and Mn^{4+} (Figure 8c). Notably, compared to the Mn $L_{II,\ III}$-edge spectra of pristine MnO_x, DH-MnO_x showed greater fractional intensity at ~641.6 eV, as well as a rather featureless L_{II} peak, indicating an increase of Mn^{4+} by calcination along with dehydration. After the cathodic reaction, the signatures associated with Mn^{4+} gave way to an intense peak at 638.6 eV (L_{III} region) and a resolved doublet at 651.4 and 649.9 eV (L_{II} region), characteristic of Mn^{2+}. The trend indicates the reduction of Mn, consistent with the structural responses in the XRD patterns. However, the only change observed after the anodic reaction (Figure 8c and S12b) was a surprising, albeit slight trend toward greater Mn^{2+}, indicating that DH-MnO_x did not substantially re-oxidize, but may have actually undergone secondary interfacial reactions. All in all, while the dehydrated compound could reduce, the reaction was not reversible, in agreement with XRD results. As a result, no Mn K-edge measurements were pursued.

Last but not least, the existence of MgO, a possible byproduct of a conversion to lower manganese oxides, was monitored by Mg K-edge XAS, scanning transmission electron

microscopy (STEM), and solid-state ^{25}Mg nuclear magnetic resonance spectroscopy (ss-NMR). The Mg K-edge spectra of the magnesiated MnO_x was much broader, with overlapping features, and had an earlier onset than the spectra of MgO, as indicated in the corresponding 1st derivative plots (Figure S15a, b).[11] The shape of the spectrum of the magnesiated oxide was similar to the signature of $Mg_xMn_{3-x}O_4$, an oxide with Mg and Mn ions, implying the presence of Mg^{2+} within the host oxide.[51] Furthermore, amorphous or poorly crystalline MgO has been reported to preserve sharp absorption peaks, which also excluded possible formation of local MgO clusters.[52, 53] No visible diamagnetic resonances at ~26 ppm, corresponding Mg^{2+} in MgO,[54] were detected, in the solid-state ^{25}Mg NMR spectra (Figure S15c), consistent with the Mg K-edge XAS analysis.

DISCUSSION

The results build a comprehensive picture that supports the existence of notable and reversible Mg^{2+} intercalation into a few-layer phyllomanganate with interlayer defects, both in half- and full-cell configurations at room temperature, distinct from the conversion reactions observed in previous literature of manganese oxides.[18, 19, 21, 24, 25, 54, 55] The structural and electronic changes as a response to intercalation were clearly evidenced by a combination of HR-XRD, electron microscopic and XAS analyses. It is intriguing that the evidence collected here differ from the reactions through conversion or extensive structural reorganization observed in birnessite.[19, 25] Aside from the obvious effect of the very small crystal sizes used in this study compared to the literature, it is tempting to speculate that the different defect chemistry of the highly exfoliated materials compared to relatively well-crystallized birnessite in the literature[19] played a role, in line with recent observations with $MgCr_2O_4$.[28] Given the rich structural

chemistry of phyllomanganate,[34, 35, 56] further studies should be dedicated to systematically explore the role of the different classes of defects on electrochemical performance.

The changes upon Mg intercalation were slightly more apparent in a full-cell experiment compared to a half-cell, but the anodic overpotentials were generally also higher, resulting in less reversibility because the cutoffs were reached faster. It was observed that the polarization in a full-cell was reduced by raising cell temperature, implying an improved kinetics of the reaction. Comparison of XAS data from different probing depths strongly suggests that the ensemble average of the surface of the electrodes reduced further than the bulk, to close to a state of Mn^{2+}. In contrast, individual particles reacted homogeneously. This gradient of oxidation states from the top to the interior of the electrode could indicate the existence of over-discharging in regions close to the electrolyte due to poor electrochemical kinetics, ion transport within the electrode or side reactions with the electrolyte. This observation hints at mechanisms of degradation, and, therefore, it deserves further attention if these systems are to be rendered viable in long term cycling. When the oxide was subject to a thermal treatment to induce water removal, it became both less electroactive and less reversible than MnO_x, implying a beneficial role of lattice water. Its properties could also be affected by the presence of small domains of α-MnO_2, as deduced from XRD, since this phase has poor electrochemical properties and undergoes conversion reactions that are limited to the surface of individual particles.[18]

CONCLUSION

In this work, the ability of exfoliated layers of a phyllomanganate to reversibly intercalate Mg^{2+} electrochemically was evaluated. High activity was observed both in half and full Mg cells, with notable degrees of reversibility even at room temperature, where ~190 mAh/g of discharge capacity were achieved. Despite a widespread decrease in capacity with cycling, the findings are encouraging in that they indicate that the reaction is not only possible, but sufficiently reversible that further incremental improvements through electrode engineering could be possible. Characterization of key electrochemical states through a combination of X-ray absorption spectroscopy, electron microscopy, and X-ray diffraction revealed structural, compositional and redox changes that were consistent with a reaction mechanism through the intercalation of Mg^{2+}. Comparison with partially dehydrated and transformed phases revealed enhanced kinetics and reversibility of the reaction within the oxide lattice in the presence of H_2O/protons in the interlayer, which is in line with current trends in the field. This study hints at the important role of defects in the electrochemical properties of phyllomanganate vis-à-vis Mg^{2+} intercalation. It also reveals incipient kinetic barriers to efficient cycling of the compounds, providing fresh new avenues of research. Our findings uncover a new candidate for a positive electrode, which could enhance the storage capability of rechargeable Mg batteries. The ability to build full Mg cells with an oxide creates an exciting path toward devices with high energy density.

EXPERIMENTAL SECTION

Phyllomanganate (MnO_x) nanoparticles were synthesized by an aqueous redox sol-gel reaction.[39] Sodium permanganate ($NaMnO_4$, Product No. 225851 in Sigma-Aldrich) was used as a precursor, and disodium salt of Fumaric acid ($C_2H_2O_4Na_2$, Product No. F1506 in Sigma-

Aldrich) was introduced as a reducing agent. A 200 ml of 0.25 M $NaMnO_4 \cdot H_2O$ solution was quickly mixed with 50 ml of 0.333 M $C_2H_2O_4Na_2$, and stirred vigorously for 1 hour at room temperature. The mixture then was sonicated for 5 hours. Following reduction, a disproportionation reaction was subsequently induced by the addition of 10 ml of 2.5 M sulfuric acid. The colloidal solution was further stirred vigorously at room temperature overnight. After washing unreacted species by centrifugation, the resultant powders were dried in a vacuum oven at 60 °C overnight. Thermal gravimetric and differential thermal analysis (TG-DTA) were carried out with a SDT-Q600 (TA instrument) in the temperature ranged from 50 to 600 ℃ at a heating rate of 5 ℃/min under synthetic air. To investigate effects of lattice water or/and absorbed water, it was partially removed by calcining the resultant powder at 400 ℃ for 3 hours in air while maintaining its structure. Throughout this manuscript, MnO_x and DH-MnO_x are used as labels for the host oxides before and after calcination, respectively.

The electrochemical performance was evaluated on composites containing the active MnO_x as working electrodes. Electrode slurries were prepared by mixing active material, carbon black (Denka), and 6 wt% of a binder solution consisting of polyvinylidene difluoride (PVDF, Kynar) in N-methylpyrrolidone (NMP, Sigma-Aldrich) to produce a dry electrode with 6:2:2 ratio. Then, the slurry was cast on a stainless steel mesh, and it was dried under vacuum at 80 ℃ overnight to evaporate NMP. The loading level of active oxide in the dry electrodes was adapted to around 1.5~2.0 mg/cm^2. Circular pieces with a diameter of 3/8 inch were punched and assembled in two-electrode coin cells in a glovebox filled with inert Ar gas where the level of water and oxygen contents were ≤ 0.1 ppm. Half-cell measurements were conducted in 0.5 M magnesium bis(trifluoromethylsulfonyl)imide ($Mg(TFSI)_2$, Solvionic, 99.5%) dissolved in 1-

butyl-1-methylpyrrolidinium bis(trifluoromethylsulfonyl)imide (PY14TFSI, Solvionic, 99.9%). The electrolyte was dried at 120 °C under vacuum for four days until the water content goes down to 43.7 ppm. The counter electrode was activated carbon cloth (ACC-5092-20, Kynol Co.), which was dried under vacuum at 110 °C overnight. The high specific surface area of the activated carbon cloth (ca. 2000 m^2g^{-1}) gives rise to sufficient double-layer charging to match the charge needed to cycle the cathode. The mass of ACC was ca. 29.3 mg and the specific capacitance was ca. 110 F g^{-1}. Full cells with a magnesium foil (GalliumSource LLC, 99.95%, 50 μm thick) with an area of 2 cm^2 were also built using 0.25 M of $Mg(CB_{11}H_{12})_2$/triglyme electrolyte, prepared according to the literature.[40, 57] The magnesium foil was scraped by a blade to expose the fresh surface of the metal in the glovebox before assembling a cell. Glass microfiber filters (VWR 28297-289) were employed as separators in the coin cell. Electrochemical measurements were performed on a Bio-Logic VMP3 at 25, 50 and 110 °C. The potentials in this report are referenced to the activated carbon cloth or Mg/Mg^{2+} couple depending on the cell configuration. The rate, *C/n*, was defined as the current density required to achieve a theoretical capacity of MnO_2, C = 270 mAh/g, in *n* hours, assuming the reaction of $0.5Mg^{2+} + MnO_2 \leftrightarrow Mg_{0.5}MnO_2$. Electrodes harvested for further characterization were washed multiple times with acetonitrile to remove electrolyte residues.

Powder X-ray diffraction was performed on a Bruker D8 Avance using Cu Kα (λ_{avg}=1.5418 Å) radiation. Scan rates were 0.04 ° s^{-1} from 10° to 80 ° (2θ). High-resolution X-ray diffraction was collected at beamlines11-ID-B or 11-BM at the Advanced Photon Source (APS), Argonne National Laboratory (ANL), with an average wavelength of 0.2114 Å (~58 keV) and 0.4127 Å (~30 keV), respectively. Samples were loaded in Kapton capillaries and mounted on

bases provided by the APS. A large amorphous silicon-based area detector (Perkin-Elmer) was used to collect high values of momentum transfer in 11-ID-B. Two platinum-striped collimating mirrors and a double-crystal Si (111) monochromator were applied for the X-ray optics in 11-BM. High resolution and short collection time are obtained by using a Si (111) crystal detector.

Transmission electron microscopy (TEM) images were obtained using a JEOL JEM 3010 operated at 300 kV. STEM imaging and EDX spectroscopy were performed on an aberration-corrected JEOL JEM-ARM200CF operated at 200 kV which can achieve a spatial resolution of ~73 pm. Images were acquired in angle annular dark field (ADF), low angle annular dark field (LAADF) and annular bright-field (ABF) modes, wherein the resulting imaging contrast is approximately Z^2. The ARM200CF is equipped with an Oxford X-Max 100TLE windowless silicon drift EDX detector.

Mn K-edge X-ray absorption near-edge structure (XANES) was performed at the MRCAT bending magnet beamline 10 at the Advanced Photon Source, Argonne National Laboratory (ANL). X-ray absorption spectra were collected in a transmission mode through the electrochemically treated ex-situ electrodes. Energy was scanned by a double-crystal Si (111) monochromator that was detuned by 50% and the incident and transmitted intensity was measured by gas ionization chambers. A Mn metal reference foil was measured simultaneously with each sample for energy calibration (Mn K-edge set to 6539 eV). Data analysis was completed using the IFEFFIT package. Mg K-edge were performed on beamline 4-ID-C at APS using a total electron yield (TEY) detector. Mn $L_{II, III}$-edge X-ray absorption spectroscopy (XAS) measurements were carried out beamline 6.3.1.2 ISAAC end station at the Advanced Light Source (ALS), Lawrence Berkeley National Laboratory. To verify the electronic environment on

the surface of the oxides, the Mn L-edge spectra were collected in a total electron yield (TEY) mode at room temperature and under ultra-high vacuum conditions (below 10^{-8} Torr). Contributions from visible light were carefully minimized before the acquisition, and all spectra were normalized by the current from freshly evaporated gold on a fine grid positioned upstream of the main chamber. The measured spectra were aligned by the beamline reference and a basic normalization using a linear background.

Solid-state ^{25}Mg magic angle spinning (MAS) NMR experiments were performed at 11.7 Tesla (500 MHz) on a Bruker Avance III spectrometer operating at a Larmor frequency of 30.64 MHz using a 3.2mm MAS probe. The spectra were acquired at a spinning speed of 20 kHz for 3.2mm rotors with a rotor synchronized spin-echo experiment (90°-τ-180°-τ) where τ is 1/r. To ensure quantification in normalized intensity experiments, single pulse experiments (data not shown) with recycle delays 0.1 to 1 seconds were used to confirm signal saturation. All ^{25}Mg shifts were referenced to 5 M $MgCl_2$ (aq.) at 0 ppm.

FIGURES

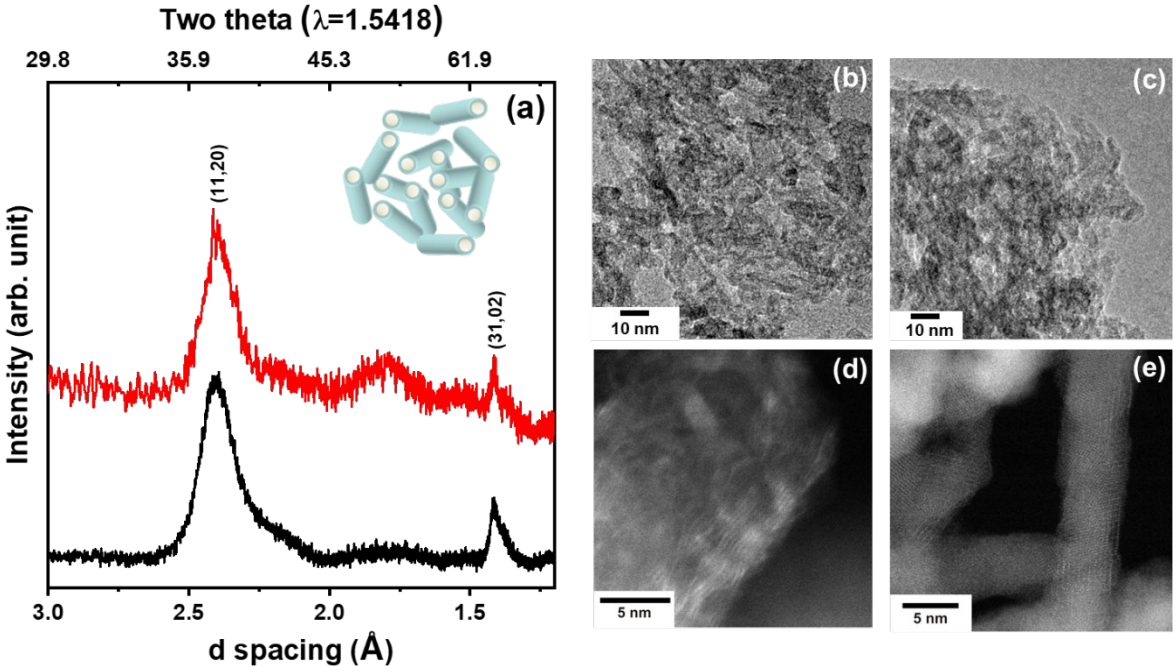

Figure 1. (a) X-ray diffraction patterns of MnO_x (black) and DH-MnO_x (red). TEM and STEM-LAADF images of (b, d) MnO_x and (c, e) DH-MnO_x. A schematic picture in Figure 1a describes the morphology of the nano-scrolls.

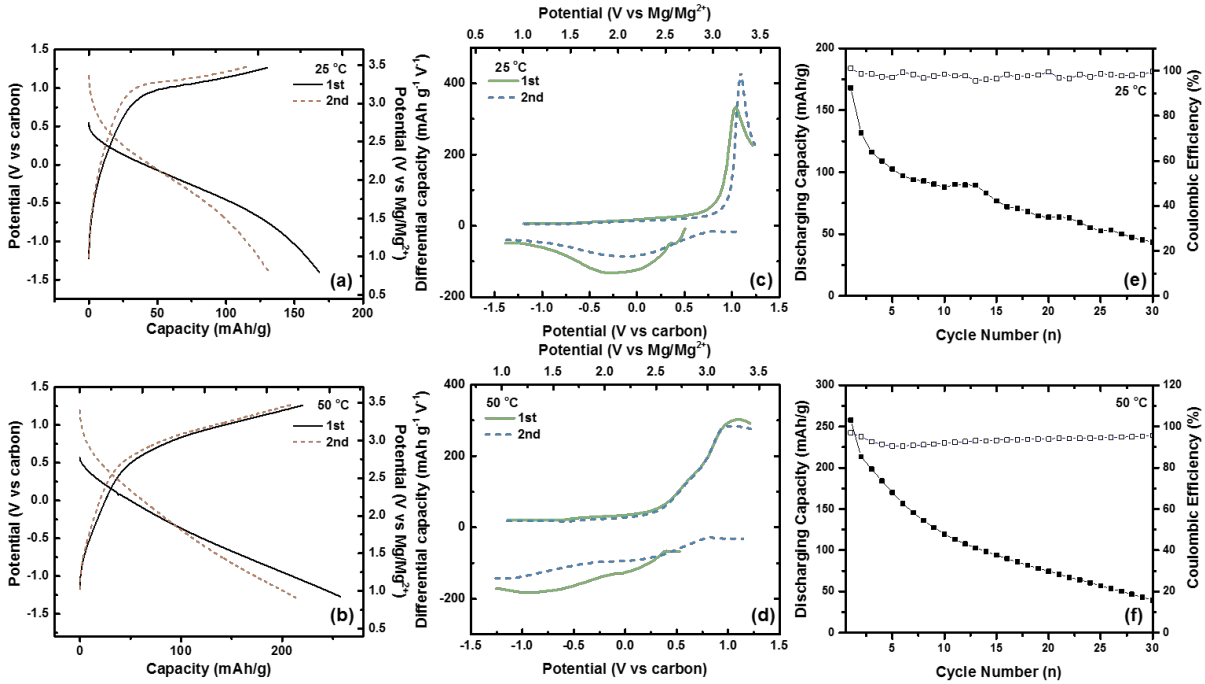

Figure 2. Potential versus capacity profiles of MnO_x cycled in 0.5 M $Mg(TFSI)_2$ electrolyte at (a) 25 ℃ and (b) 50 ℃, and (c, d) the corresponding dQ/dV plots of the reactions. Cycling performance of the cathodes at C/50 rate at (e) 25 ℃ and (f) 50 ℃.

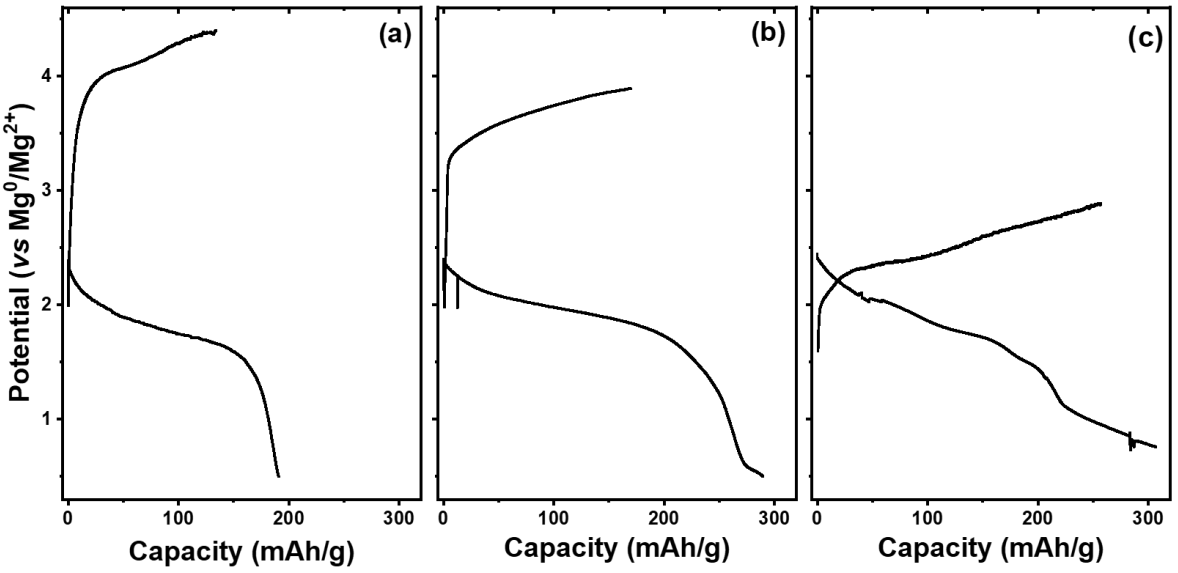

Figure 3. Potential versus capacity profiles of MnO_x paired with a Mg metal anode in 0.25 M $Mg(CB_{11}H_{12})_2$ at (a) 25 ℃, (b) 50 ℃ and (c) 110 ℃.

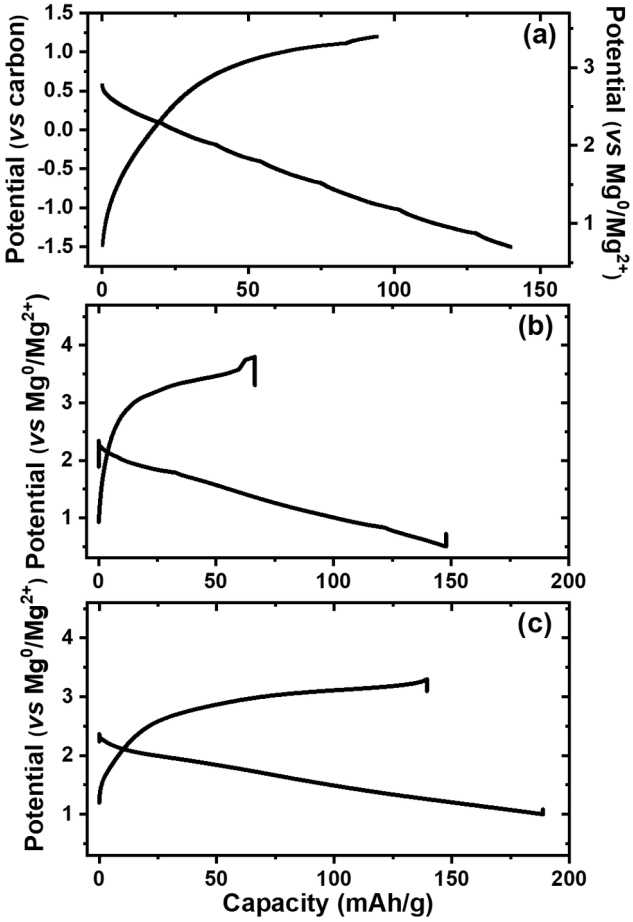

Figure 4. Potential versus capacity profiles of DH-MnO_x in (a) a half-cell at 25 ℃ and a full-cell at (b) 25 ℃ and (c) 50 ℃, respectively.

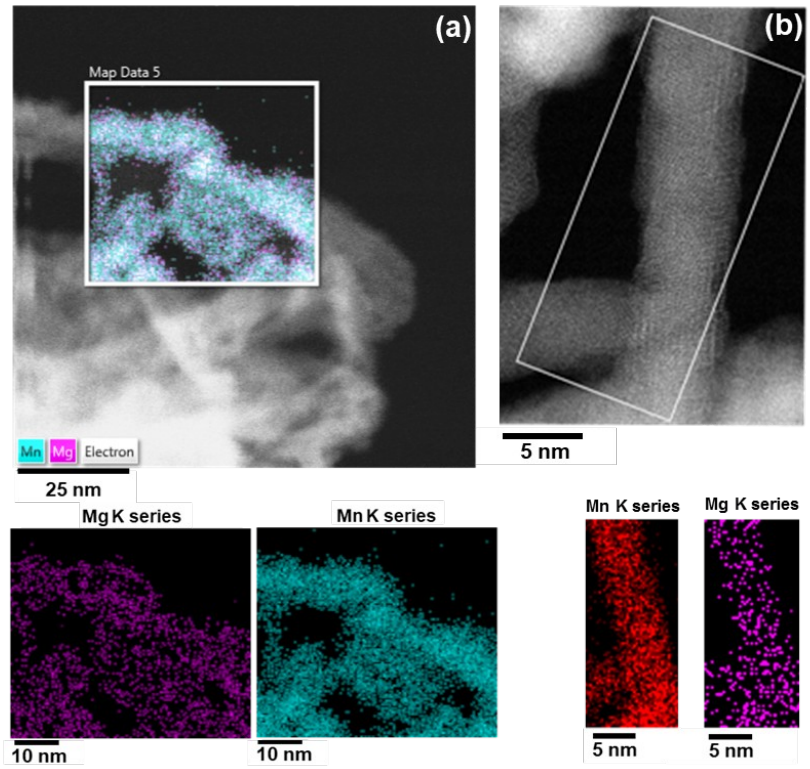

Figure 5. Elemental maps of (a) magnesiated MnO_x nanoparticles prepared in a full-cell at 25 ℃ and (b) magnesiated DH-MnO_x cycled in a full-cell at 50 ℃.

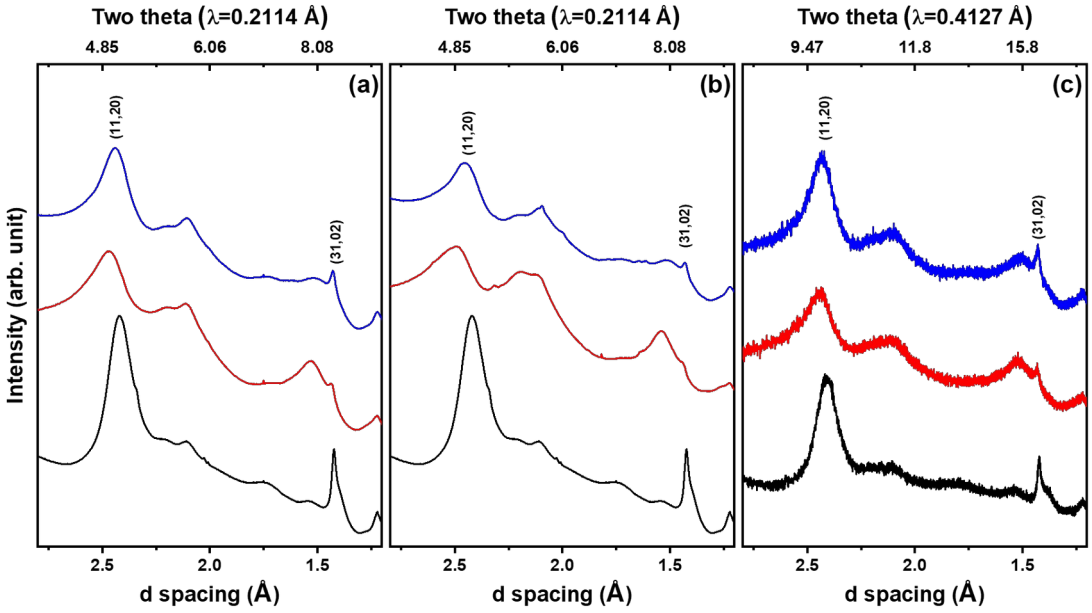

Figure 6. Synchrotron XRD patterns of pristine, discharged, and charged MnO_x electrodes harvested from (a) a half-cell and (b) a full-cell at 25 ℃. (c) Synchrotron XRD of DH-MnO_x electrodes harvested from a full-cell at 50 ℃. (Pristine: black, discharged: red and charged state: blue)

Table 1. Estimated *d* spacing on the planes at different states of charges corresponding to the diffraction patterns in Figure 6.

	MnO_X in a half-cell		MnO_X in a full-cell		DH-MnO_X in a full-cell	
	d spacing (11, 20)	*d* spacing (31, 02)	*d* spacing (11, 20)	*d* spacing (31, 02)	*d* spacing (11, 20)	*d* spacing (31, 02)
Pristine	2.416	1.420	2.416	1.420	2.410	1.420
Discharged state	2.470	1.430	2.489	1.440	2.451	1.440
Charged state	2.430	1.425	2.449	1.428	2.447	1.434

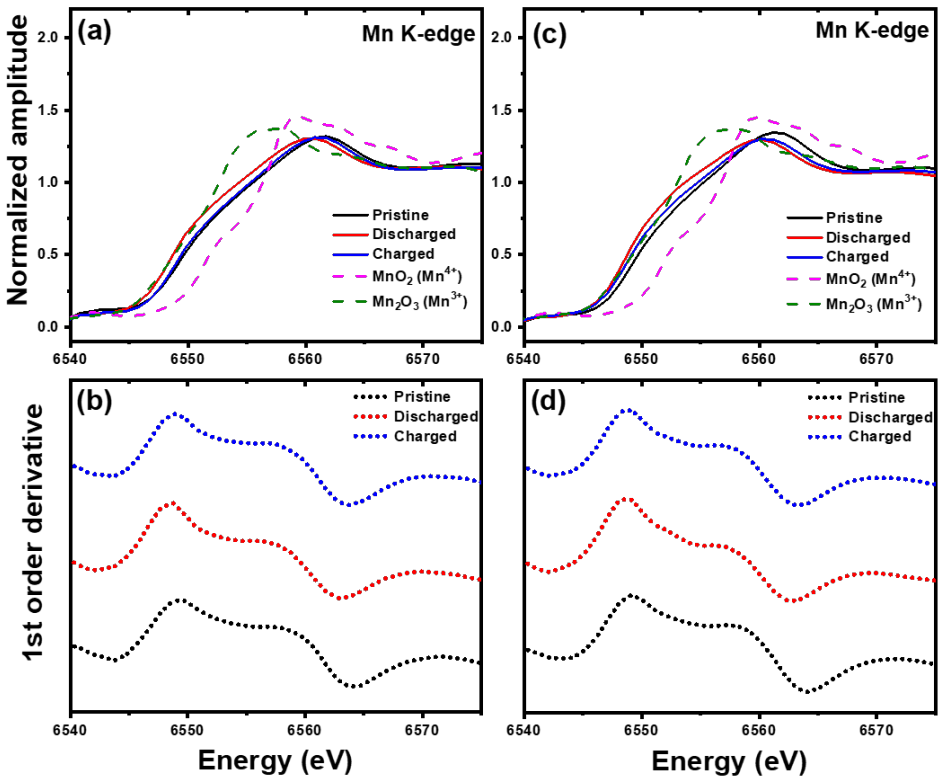

Figure 7. Mn K-edge XAS and corresponding first-order derivative plots of MnO_x electrodes at different states of charges prepared in (a, b) a half-cell and (c, d) full-cell at 25 ℃.

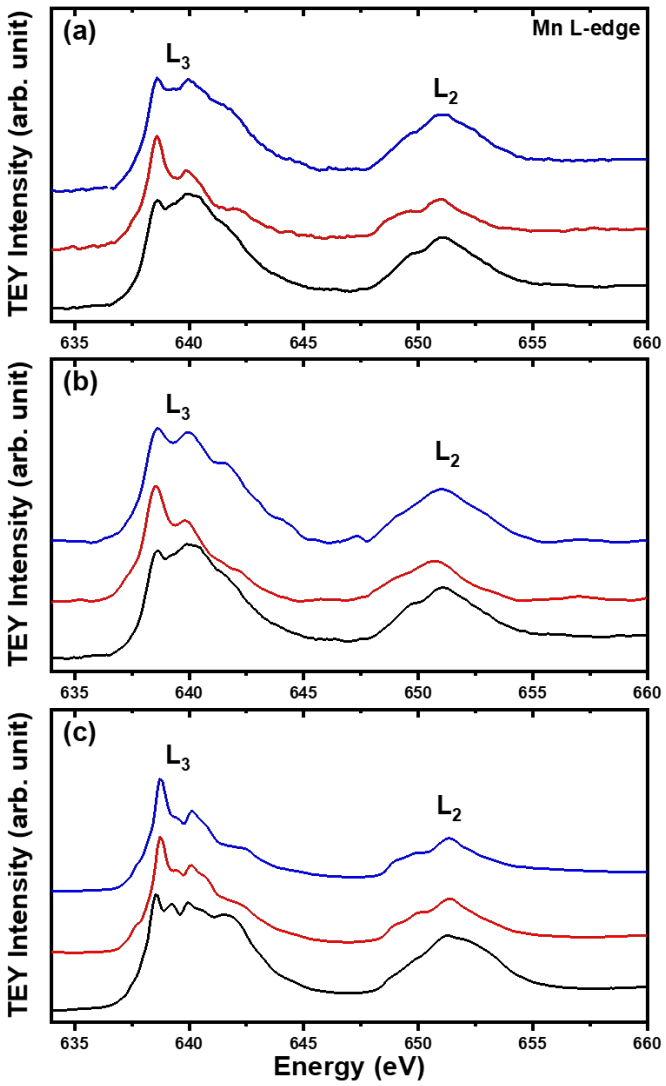

Figure 8. Mn L-edge XAS of MnO_x electrodes at different states of charges prepared in (a) a half-cell and (b) full-cell at 25 ℃, and (c) DH-MnO_x cycled in a full-cell at 50 ℃. (Pristine: black, discharged: red and charged electrode: blue)

ASSOCIATED CONTENT

Supporting Information

The following files are available free of charge.

HR-XRD patterns of MnO_x, thermal gravimetric analysis, XRD patterns of DH-MnO_x and calcined DH-MnO_x in TG-DTA measurement, potential versus capacity profile in a half-cell at different rates of reaction, charging/discharging curves of MnO_x in $Mg(TFSI)_2$ electrolyte, discharging curves at variable temperatures, TEM-EDX spectrum of different states of charges in MnO_x, STEM-EDX spectra of magnesiated DH-MnO_x, X-ray diffraction patterns of pristine powder and electrode composite, diffraction patterns at wide angles corresponding to Figure 6, table for energy threshold E_0 values of different electrochemical states of MnO_x, Mn $L_{II, III}$-edge spectra of standard Mn-oxides, overlaid Mn L_{III} spectra of different states of charge, Mn L-edge spectra over the magnesiated MnO_x nanoparticle, representative Mn L- and O K-edge of the pristine and magnesiated MnO_x, Mg K-edge spectra of MgO and discharged MnO_x and solid state ^{25}Mg NMR spectra.

AUTHOR INFORMATION

Corresponding Author

*E-mail: jcabana@uic.edu

Author Contributions

BJK, CK and JC designed the project. JJ and RFK captured electron microscopic images. BJK, HDY, CL and SH performed electrochemical experiments. SH, YL and JG collected X-ray absorption spectra. BK and CK made scientific comments on the draft. BJK and JC wrote the manuscript. The manuscript was written through contributions of all authors. All authors have given approval to the final version of the manuscript.

Notes

The authors declare no competing financial interest.

ACKNOWLEDGMENTS

This work is supported by the Joint Center for Energy Storage Research (JCESR) of the U.S. Department of Energy (DOE). This work made use of instruments in the Electron Microcopy Service, specifically JEOL JEM-ARM200CF in the Research Resources Center, University of Illinois at Chicago. Use of the Advanced Photon Source at Argonne National Laboratory was supported by the U.S. Department of Energy, Office of Science, Office of Basic Energy Sciences, under Contract No. DE-AC02-06CH11357. This research used resources of the Advanced Light Source, which is a DOE Office of Science User Facility under Contract No. DE-AC02-05CH11231.

REFERENCES

1. Muldoon, J.; Bucur, C. B.; Gregory, T., Quest for Nonaqueous Multivalent Secondary Batteries: Magnesium and Beyond. *Chem Rev* **2014,** *114* (23), 11683-11720.
2. Levi, E.; Gofer, Y.; Aurbach, D., On the Way to Rechargeable Mg Batteries: The Challenge of New Cathode Materials. *Chem Mater* **2010,** *22* (3), 860-868.
3. Song, J.; Sahadeo, E.; Noked, M.; Lee, S. B., Mapping the Challenges of Magnesium Battery. *J Phys Chem Lett* **2016,** *7* (9), 1736-1749.
4. Mao, M. L.; Gao, T.; Hou, S. Y.; Wang, C. S., A critical review of cathodes for rechargeable Mg batteries. *Chem Soc Rev* **2018,** *47* (23), 8804-8841.
5. Ichitsubo, T.; Adachi, T.; Yagi, S.; Doi, T., Potential positive electrodes for high-voltage magnesium-ion batteries. *J Mater Chem* **2011,** *21* (32), 11764-11772.
6. Kim, C.; Phillips, P. J.; Key, B.; Yi, T. H.; Nordlund, D.; Yu, Y. S.; Bayliss, R. D.; Han, S. D.; He, M. N.; Zhang, Z. C.; Burrell, A. K.; Klie, R. F.; Cabana, J., Direct Observation of Reversible Magnesium Ion Intercalation into a Spinel Oxide Host. *Adv Mater* **2015,** *27* (22), 3377-3384.
7. Canepa, P.; Gautam, G. S.; Hannah, D. C.; Malik, R.; Liu, M.; Gallagher, K. G.; Persson, K. A.; Ceder, G., Odyssey of Multivalent Cathode Materials: Open Questions and Future Challenges. *Chem Rev* **2017,** *117* (5), 4287-4341.
8. Sun, X. Q.; Bonnick, P.; Duffort, V.; Liu, M.; Rong, Z. Q.; Persson, K. A.; Ceder, G.; Nazar, L. F., A high capacity thiospinel cathode for Mg batteries. *Energ Environ Sci* **2016,** *9* (7), 2273-2277.
9. Shan, P.; Gu, Y.; Yang, L. Y.; Liu, T. C.; Zheng, J. X.; Pan, F., Olivine FePO4 Cathode Material for Rechargeable Mg-Ion Batteries. *Inorg Chem* **2017,** *56* (21), 13411-13416.
10. Rodriguez-Perez, I. A.; Yuan, Y. F.; Bommier, C.; Wang, X. F.; Ma, L.; Leonard, D. P.; Lerner, M. M.; Carter, R. G.; Wu, T. P.; Greaney, P. A.; Lu, J.; Ji, X. L., Mg-Ion Battery Electrode: An Organic Solid's Herringbone Structure Squeezed upon Mg-Ion Insertion. *J Am Chem Soc* **2017,** *139* (37), 13031-13037.
11. Yoo, H. D.; Jokisaari, J. R.; Yu, Y. S.; Kwon, B. J.; Hu, L. H.; Kim, S.; Han, S. D.; Loyez, M.; Lapidus, S. H.; Nolis, G. M.; Ingram, B. J.; Bolotin, I.; Ahmed, S.; Klie, R. F.; Vaughey, J. T.; Fister, T. T.; Cabana, J., Intercalation of Magnesium into a Layered Vanadium Oxide with High Capacity. *Acs Energy Lett* **2019,** *4* (7), 1528-1534.
12. Andrews, J. L.; Mukherjee, A.; Yoo, H. D.; Parija, A.; Marley, P. M.; Fakra, S.; Prendergast, D.; Cabana, J.; Klie, R. F.; Banerjee, S., Reversible Mg-Ion Insertion in a Metastable One-Dimensional Polymorph of V2O5. *Chem-Us* **2018,** *4* (3), 564-585.
13. Aurbach, D.; Lu, Z.; Schechter, A.; Gofer, Y.; Gizbar, H.; Turgeman, R.; Cohen, Y.; Moshkovich, M.; Levi, E., Prototype systems for rechargeable magnesium batteries. *Nature* **2000,** *407* (6805), 724-727.
14. Chen, T. N.; Gautam, G. S.; Huang, W. X.; Ceder, G., First-Principles Study of the Voltage Profile and Mobility of Mg Intercalation in a Chromium Oxide Spinel. *Chem Mater* **2018,** *30* (1), 153-162.

15. Rong, Z. Q.; Malik, R.; Canepa, P.; Gautam, G. S.; Liu, M.; Jain, A.; Persson, K.; Ceder, G., Materials Design Rules for Multivalent Ion Mobility in Intercalation Structures. *Chem Mater* **2015,** *27* (17), 6016-6021.
16. Hannah, D. C.; Gautam, G. S.; Canepa, P.; Ceder, G., On the Balance of Intercalation and Conversion Reactions in Battery Cathodes. *Adv Energy Mater* **2018,** *8* (20).
17. Liu, M.; Rong, Z. Q.; Malik, R.; Canepa, P.; Jain, A.; Ceder, G.; Persson, K. A., Spinel compounds as multivalent battery cathodes: a systematic evaluation based on ab initio calculations. *Energ Environ Sci* **2015,** *8* (3), 964-974.
18. Arthur, T. S.; Zhang, R. G.; Ling, C.; Glans, P. A.; Fan, X. D.; Guo, J. H.; Mizuno, F., Understanding the Electrochemical Mechanism of K-alpha MnO2 for Magnesium Battery Cathodes. *Acs Appl Mater Inter* **2014,** *6* (10), 7004-7008.
19. Sun, X. Q.; Duffort, V.; Mehdi, B. L.; Browning, N. D.; Nazar, L. F., Investigation of the Mechanism of Mg Insertion in Birnessite in Nonaqueous and Aqueous Rechargeable Mg-Ion Batteries. *Chem Mater* **2016,** *28* (2), 534-542.
20. Han, S. D.; Kim, S.; Li, D. G.; Petkov, V.; Yoo, H. D.; Phillips, P. J.; Wang, H.; Kim, J. J.; More, K. L.; Key, B.; Klie, R. F.; Cabana, J.; Stamenkovic, V. R.; Fister, T. T.; Markovic, N. M.; Burrell, A. K.; Tepavcevic, S.; Vaughey, J. T., Mechanism of Zn Insertion into Nanostructured delta-MnO2: A Nonaqueous Rechargeable Zn Metal Battery. *Chem Mater* **2017,** *29* (11), 4874-4884.
21. Zhang, R. G.; Yu, X. Q.; Nam, K. W.; Ling, C.; Arthur, T. S.; Song, W.; Knapp, A. M.; Ehrlich, S. N.; Yang, X. Q.; Matsui, M., alpha-MnO2 as a cathode material for rechargeable Mg batteries. *Electrochem Commun* **2012,** *23*, 110-113.
22. Post, J. E., Manganese oxide minerals: Crystal structures and economic and environmental significance. *P Natl Acad Sci USA* **1999,** *96* (7), 3447-3454.
23. Ji, X.; Chen, J.; Wang, F.; Sun, W.; Ruan, Y. J.; Miao, L.; Jiang, J. J.; Wang, C. S., Water-Activated VOPO4 for Magnesium Ion Batteries. *Nano Lett* **2018,** *18* (10), 6441-6448.
24. Song, J.; Noked, M.; Gillette, E.; Duay, J.; Rubloff, G.; Lee, S. B., Activation of a MnO2 cathode by water-stimulated Mg2+ insertion for a magnesium ion battery. *Phys Chem Chem Phys* **2015,** *17* (7), 5256-5264.
25. Nam, K. W.; Kim, S.; Lee, S.; Salama, M.; Shterenberg, I.; Gofer, Y.; Kim, J. S.; Yang, E.; Park, C. S.; Kim, J. S.; Lee, S. S.; Chang, W. S.; Doo, S. G.; Jo, Y. N.; Jung, Y.; Aurbach, D.; Choi, J. W., The High Performance of Crystal Water Containing Manganese Birnessite Cathodes for Magnesium Batteries. *Nano Lett* **2015,** *15* (6), 4071-4079.
26. Novak, P.; Desilvestro, J., Electrochemical Insertion of Magnesium in Metal-Oxides and Sulfides from Aprotic Electrolytes. *J Electrochem Soc* **1993,** *140* (1), 140-144.
27. Gautam, G. S.; Canepa, P.; Urban, A.; Bo, S. H.; Ceder, G., Influence of Inversion on Mg Mobility and Electrochemistry in Spinels. *Chem Mater* **2017,** *29* (18), 7918-7930.
28. Hu, L. H.; Johnson, I. D.; Kim, S.; Nolis, G. M.; Freeland, J. W.; Yoo, H. D.; Fister, T. T.; McCafferty, L.; Ashton, T. E.; Darr, J. A.; Cabana, J., Tailoring the electrochemical activity of magnesium chromium oxide towards Mg batteries through control of size and crystal structure. *Nanoscale* **2019,** *11* (2), 639-646.
29. Drits, V. A.; Lanson, B.; Gaillot, A. C., Birnessite polytype systematics and identification by powder X-ray diffraction. *Am Mineral* **2007,** *92* (5-6), 771-788.

30. Aldi, K. A.; Cabana, J.; Sideris, P. J.; Grey, C. P., Investigation of cation ordering in triclinic sodium birnessite via Na-23 MAS NMR spectroscopy. *Am Mineral* **2012,** *97* (5-6), 883-889.
31. Yang, X. J.; Makita, Y.; Liu, Z. H.; Sakane, K.; Ooi, K., Structural characterization of self-assembled MnO2 nanosheets from birnessite manganese oxide single crystals. *Chem Mater* **2004,** *16* (26), 5581-5588.
32. Sa, N.; Kinnibrugh, T. L.; Wang, H.; Gautam, G. S.; Chapman, K. W.; Vaughey, J. T.; Key, B.; Fister, T. T.; Freeland, J. W.; Proffit, D. L.; Chupas, P. J.; Ceder, G.; Bareno, J. G.; Bloom, I. D.; Burrell, A. K., Structural Evolution of Reversible Mg Insertion into a Bilayer Structure of V2O5 center dot nH(2)O Xerogel Material. *Chem Mater* **2016,** *28* (9), 2962-2969.
33. Zhu, M. Q.; Ginder-Vogel, M.; Parikh, S. J.; Feng, X. H.; Sparks, D. L., Cation Effects on the Layer Structure of Biogenic Mn-Oxides. *Environ Sci Technol* **2010,** *44* (12), 4465-4471.
34. Grangeon, S.; Fernandez-Martinez, A.; Warmont, F.; Gloter, A.; Marty, N.; Poulain, A.; Lanson, B., Cryptomelane formation from nanocrystalline vernadite precursor: a high energy X-ray scattering and transmission electron microscopy perspective on reaction mechanisms. *Geochem T* **2015,** *16*.
35. Manceau, A.; Marcus, M. A.; Grangeon, S.; Lanson, M.; Lanson, B.; Gaillot, A. C.; Skanthakumar, S.; Soderholm, L., Short-range and long-range order of phyllomanganate nanoparticles determined using high-energy X-ray scattering. *J Appl Crystallogr* **2013,** *46*, 193-209.
36. Silvester, E.; Manceau, A.; Drits, V. A., Structure of synthetic monoclinic Na-rich birnessite and hexagonal birnessite .2. Results from chemical studies and EXAFS spectroscopy. *Am Mineral* **1997,** *82* (9-10), 962-978.
37. Villalobos, M.; Toner, B.; Bargar, J.; Sposito, G., Characterization of the manganese oxide produced by Pseudomonas putida strain MnB1. *Geochim Cosmochim Ac* **2003,** *67* (14), 2649-2662.
38. Jurgensen, A.; Widmeyer, J. R.; Gordon, R. A.; Bendell-Young, L. I.; Moore, M. M.; Crozier, E. D., The structure of the manganese oxide on the sheath of the bacterium Leptothrix discophora: An XAFS study. *Am Mineral* **2004,** *89* (7), 1110-1118.
39. Xu, J. J.; Kinser, A. J.; Owens, B. B.; Smyrl, W. H., Amorphous manganese dioxide: A high capacity lithium intercalation host. *Electrochem Solid St* **1998,** *1* (1), 1-3.
40. Tutusaus, O.; Mohtadi, R.; Arthur, T. S.; Mizuno, F.; Nelson, E. G.; Sevryugina, Y. V., An Efficient Halogen-Free Electrolyte for Use in Rechargeable Magnesium Batteries. *Angew Chem Int Edit* **2015,** *54* (27), 7900-7904.
41. Carter, T. J.; Mohtadi, R.; Arthur, T. S.; Mizuno, F.; Zhang, R. G.; Shirai, S.; Kampf, J. W., Boron Clusters as Highly Stable Magnesium-Battery Electrolytes. *Angew Chem Int Edit* **2014,** *53* (12), 3173-3177.
42. Tutusaus, O.; Mohtadi, R.; Singh, N.; Arthur, T. S.; Mizuno, F., Study of Electrochemical Phenomena Observed at the Mg Metal/Electrolyte Interface. *Acs Energy Lett* **2017,** *2* (1), 224-229.
43. Kuwata, H.; Matsui, M.; Imanishi, N., Passivation Layer Formation of Magnesium Metal Negative Electrodes for Rechargeable Magnesium Batteries. *J Electrochem Soc* **2017,** *164* (13), A3229-A3236.

44. Webb, S. M.; Tebo, B. M.; Bargat, J. R., Structural characterization of biogenic Mn oxides produced in seawater by the marine bacillus sp strain SG-1. *Am Mineral* **2005,** *90* (8-9), 1342-1357.
45. Zhao, H. Y.; Zhu, M. Q.; Li, W.; Elzinga, E. J.; Villalobos, M.; Liu, F.; Zhang, J.; Feng, X. H.; Sparks, D. L., Redox Reactions between Mn(II) and Hexagonal Birnessite Change Its Layer Symmetry. *Environ Sci Technol* **2016,** *50* (4), 1750-1758.
46. Drits, V. A.; Silvester, E.; Gorshkov, A. I.; Manceau, A., Structure of synthetic monoclinic Na-rich birnessite and hexagonal birnessite .1. Results from X-ray diffraction and selected-area electron diffraction. *Am Mineral* **1997,** *82* (9-10), 946-961.
47. Liu, R. S.; Jang, L. Y.; Chen, J. M.; Tsai, Y. C.; Hwang, Y. D.; Liu, R. G., X-ray absorption studies in spinel-type LiMn2O4. *J Solid State Chem* **1997,** *128* (2), 326-329.
48. Risch, M.; Stoerzinger, K. A.; Han, B. H.; Regier, T. Z.; Peak, D.; Sayed, S. Y.; Wei, C.; Xu, Z. C.; Shao-Horn, Y., Redox Processes of Manganese Oxide in Catalyzing Oxygen Evolution and Reduction: An in Situ Soft X-ray Absorption Spectroscopy Study. *J Phys Chem C* **2017,** *121* (33), 17682-17692.
49. Grush, M. M.; Horne, C. R.; Perera, R. C. C.; Ederer, D. L.; Cramer, S. P.; Cairns, E. J.; Callcott, T. A., Correlating electronic structure with cycling performance of substituted LiMn2O4 electrode materials: A study using the techniques of soft X-ray absorption and emission. *Chem Mater* **2000,** *12* (3), 659-664.
50. Laffont, L.; Gibot, P., High resolution electron energy loss spectroscopy of manganese oxides: Application to Mn3O4 nanoparticles. *Mater Charact* **2010,** *61* (11), 1268-1273.
51. Kim, C.; Adil, A. A.; Bayliss, R. D.; Kinnibrugh, T. L.; Lapidus, S. H.; Nolis, G. M.; Freeland, J. W.; Phillips, P. J.; Yi, T. H.; Yoo, H. D.; Kwon, B. J.; Yu, Y. S.; Klie, R.; Chupas, P. J.; Chapman, K. W.; Cabana, J., Multivalent Electrochemistry of Spinel MgxMn3-xO4 Nanocrystals. *Chem Mater* **2018,** *30* (5), 1496-1504.
52. Singh, J. P.; Kim, S. H.; Won, S. O.; Lee, I. J.; Chae, K. H., Atomic-scale investigation of MgO growth on fused quartz using angle-dependent NEXAFS measurements. *Rsc Adv* **2018,** *8* (55), 31275-31286.
53. Yoshida, T.; Tanaka, T.; Yoshida, H.; Funabiki, T.; Yoshida, S.; Murata, T., Study of Dehydration of Magnesium-Hydroxide. *J Phys Chem-Us* **1995,** *99* (27), 10890-10896.
54. Wang, H.; Senguttuvan, P.; Proffit, D. L.; Pan, B. F.; Liao, C.; Burrell, A. K.; Vaughey, J. T.; Key, B., Formation of MgO during Chemical Magnesiation of Mg-Ion Battery Materials. *Ecs Electrochem Lett* **2015,** *4* (8).
55. Zhang, R.; Arthur, T. S.; Ling, C.; Mizuno, F., Manganese dioxides as rechargeable magnesium battery cathode; synthetic approach to understand magnesiation process. *J Power Sources* **2015,** *282*, 630-638.
56. Grangeon, S.; Lanson, B.; Miyata, N.; Tani, Y.; Manceau, A., Structure of nanocrystalline phyllomanganates produced by freshwater fungi. *Am Mineral* **2010,** *95* (11-12), 1608-1616.
57. McArthur, S. G.; Geng, L. X.; Guo, J. C.; Lavallo, V., Cation reduction and comproportionation as novel strategies to produce high voltage, halide free, carborane based electrolytes for rechargeable Mg batteries. *Inorg Chem Front* **2015,** *2* (12), 1101-1104.

Table of Contents graphic